IEEJ TRANSACTIONS ON ELECTRICAL AND ELECTRONIC ENGINEERING
IEEJ Trans 2018; **13**: 505–509
Published online in Wiley Online Library (wileyonlinelibrary.com). DOI:10.1002/tee.22594

Paper

Rail Surface Spalling Detection Based on Visual Saliency

Zhixin Hu[*,**,a], Non-member
Hongtao Zhu[*], Non-member
Ming Hu[***], Non-member
Yong Ma[****], Non-member

The rail surface images captured by line-scan cameras are susceptible to nonuniform illumination, stray light, smoothness variations of the rail surface, and so on, which degrade the detection accuracy of the rail surface spalling. To solve this problem, we propose an optical rail surface spalling detection algorithm based on visual saliency. First, the rail surface area is located to eliminate the interference of the surrounding area. Then, a two-dimensional difference of Gaussian (2D DoG) filter is used to reduce the noise. The filtered images are processed by means of a block local contrast measure (BLCM) estimator, which enhances the contrast of the spalling areas and produces the saliency map. Finally, a threshold is applied to locate the spalling areas. Experimental results demonstrate that the proposed algorithm achieves a detection accuracy of 93.5% and shows good robustness under nonuniform illumination and various rail surface smoothness conditions. © 2018 Institute of Electrical Engineers of Japan. Published by John Wiley & Sons, Inc.

Keywords: rail surface spalling; defect detection; visual saliency; block local contrast measure (BLCM); robustness

Received 15 November 2016; Revised 7 June 2017

1. Introduction

Rail surface spalling, generally originating from surface fatigue cracks, is one of the prominent rail defects that affect the safety of train operations. In its first stage, spalling may cause damage to the train wheels and axles; moreover, in some cases cracks can grow down into the rail, and further deterioration of spalling could cause the rail to break, which is highly dangerous if not detected [1–3]. Among the commonly used rail inspection techniques [4], ultrasonic inspection has the problem of 'blind spots', and may become untestable in the presence of large subsurface cracks [5–7]; eddy current techniques suffer from low precision and interference from rail surface conditions [8]. On the other hand, the newly emerged computer vision-based optical rail surface spalling inspection has become popular in recent years [9]. In this technique, images of rail surfaces are first obtained by cameras, and these images are then analyzed by computer vision algorithms to automatically identify and locate the spalling areas [10–13].

There are mainly two types of computer vision algorithms used in rail surface spalling detection. One employs the K-nearest neighbor classifier [14] or gray scale histogram [15] to recognize and locate the texture difference between normal surface and spalling areas. But this texture-based method has limited precision due to the random distributions and shapes of the spalling spots. The other method carries out threshold segmentation based on the gray scale difference, and then locate the spalling areas by morphological algorithms [16]. As the precision of threshold segmentation may be influenced by nonuniform illumination, several improved algorithms based on nonlinear local contrast enhancement [17] and dynamic threshold segmentation [18] have been proposed lately.

However, current computer vision-based algorithms still meet the challenge of degraded precision due to lack of illumination uniformity, stray light, smoothness variation of the rail surface, etc. To improve the accuracy and robustness of rail surface spalling detection, in this paper we introduce visual saliency, which is inspired by the scene-dependent human visual system model proposed by Itti and Koch [19,20], to the process of spalling detection. According to this model, a spot with high contrast is easier to draw a person's attention compared to a larger area with changed brightness. By taking advantage of this feature, it is possible to eliminate the nonuniform illumination and other influences, and hence improve the accuracy of detection. Chen *et al.* introduced a highly efficient local contrast measure algorithm [21] in this model to improve the precision for finding small targets, and Sharma introduced a group-based asymmetry algorithm [22] to improve the computation speed of the saliency map. But these algorithms still have difficulty in distinguishing grain noises or nonuniform illumination from real spalling spots.

In order to address these problems, an improved optical detection algorithm based on visual saliency is proposed in this paper. First, Canny operator and Hough transformation are implemented to locate the boundary of the rail surface and avoid the influence of irrelevant surrounding area. Then a two-dimensional difference of Gaussian (2D DoG) filter is used to reduce the noise and enhance the contrast between normal and spalling areas. The filtered images are processed by a block local contrast measure (BLCM) estimator to produce the saliency map. Finally, a threshold is applied to automatically locate the spalling area.

2. Algorithm Mechanism

2.1. Rail surface positioning Rail images obtained by cameras usually contain irrelevant surrounding areas which should be eliminated to avoid unnecessary interference. Therefore, the first step of the algorithm is to locate the edge positions of the rail

[a] Correspondence to: Zhixin Hu. E-mail: jasonhu928@163.com

[*] School of Mechanical and Electrical Engineering, Nanchang University, Nanchang, Jiangxi Province, China
[**] School of Mechanical and Vehicular Engineering, Nanchang Institute of Science and Technology, Nanchang, Jiangxi Province, China
[***] College of Electrical & Information Engineering, Nanchang Institute of Science and Technology, Nanchang, Jiangxi Province, China
[****] Electronic Information School, Wuhan University, Wuhan, Hubei Province, China

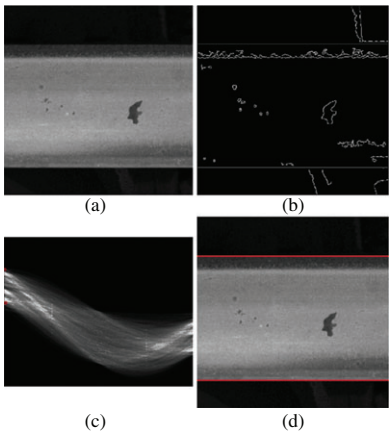

Fig. 1. The procedure of rail surface positioning: (a) original image, (b) image processed by Canny operator, (c) the result of Hough transformation, and (d) the result of rail surface positioning

surface in the image. Generally, this is realized by edge extraction operators such as Roberts, Sobel, Prewitt, Canny, and so on. Among them, the Canny operator finds the intensity discontinuities in an image, and is most suitable for rail boundary positioning, which requires good continuity.

After edge extraction, the boundaries of rail surface appear as two obvious straight lines, which could be recognized from the original image via Hough transformation. The Hough transformation clusters the collinear points in the image space, and is robust to detect discontinuous edges that are interrupted by noise or damage.

By mapping each point in the original image into the parameter space, we can obtain the Hough transformation parameter space. Then the boundaries of the rail surface can be obtained by finding the two points with the maximum overlapping counts:

$$\rho_a = x\cos\theta_a + y\cos\theta_a,\ \rho_a = x\cos\theta_b + y\sin\theta_b \tag{1}$$

where (x,y) is the Cartesian coordinate of the original image, and (ρ_a,θ_a) and (ρ_b,θ_b) are the coordinates of the boundaries in the parameter space.

As in real applications the position of the rail surface tends to stay unchanged during multiple frames, it is usually not necessary to perform rail surface positioning for each single frame; instead, a boundary recalibration after each ten frames will be fair enough.

The procedure of rail surface positioning is shown in Fig. 1.

As can be seen from the original image in Fig. 1(a), due to the curvature of the rail surface and the nonparallel illumination angle, there are several black and white dividing lines along the rail. Thus the brightness contrast of the rail surface boundaries may not be the strongest, so traditional methods based simply on binarization or contrast detection may acquire wrong boundaries. Our boundary detection method is based on the statistical result of the long parallel lines in the image, so it is insusceptible to other dividing lines.

2.2. Rail surface spalling detection

2.2.1. 2D DoG filter The first step of spalling detection is noise reduction, which is conducted through filters. The 2D DoG filter can eliminate grain noise, suppress background, enhance target, and mitigate the influence of nonuniform illumination, so it is very suitable for visual saliency systems [23]. The definition of 2D DoG template is

$$\begin{aligned} DOG(i,j,\sigma_u,\sigma_l) &= \frac{1}{2\pi}\frac{1}{\sigma_u^2}\exp\left(-\frac{i^2+j^2}{2\sigma_u^2}\right) \\ &\quad -\frac{1}{2\pi}\frac{1}{\sigma_l^2}\exp\left(-\frac{i^2+j^2}{2\sigma_l^2}\right) \\ &= T_u - T_l, \quad \sigma_u < \sigma_l \end{aligned} \tag{2}$$

where σ_u and σ_l are the standard deviations of two-dimensional Gaussian distribution, and T_u and T_l are the upper and lower limit of the filtering template, respectively.

The 2D DoG filter is a band-pass filter, and a key problem is how to determine the upper and lower cut-off frequency f_u and f_l. The ideal 2D DoG filter should satisfy

$$f_b < f_l < f_t < f_u < f_n \tag{3}$$

where f_b, f_t, and f_n are the cut-off frequencies of the background, spalling area, and noise, respectively. Because of the complexity and unpredictability of the actual scene, the range of target frequency is hard to predict. Here we let $f_l \to 0$ to protect the target; thus the lower limit filtering template degenerates into a mean template. On the other hand, the upper limit template is set according to Ref. [23].

After 2D DoG filtering, the output image becomes

$$I_0 = |I_i * T_u - I_i * T_l| \tag{4}$$

where I_i is the original input image, and I_o is the output image after 2D DoG filtering. 2D DoG filtering reduces the difference caused by nonuniformity of illumination prominently; it smooths out the grain noise and enhances the contrast between the spalling areas and normal areas.

2.2.2. Block local contrast measure The establishment of the saliency map is the core part of the detection. Traditional visual saliency algorithms based on pixel contrast [21] or group asymmetry [22] are either sensitive to point targets or specific groups. Thus they are easily affected by grain noises or nonuniform illumination. To achieve better detection accuracy, we propose a novel saliency algorithm based on the particular properties of the spalling areas.

According to Ref. [1], a spalling area is deemed as slight damage if its length is more than 15 mm, as severe damage if it is more than 30 mm, and as breakage if it is more than 50 mm. According to these criteria, only targets with a certain size should be noteworthy in the saliency map. Taking this into consideration, we propose the BLCM algorithm. First we divide the image into blocks of certain sizes and then compute the block local contrast of each block. In this way, minor spots or noises will be ignored, and the computational speed will also be increased significantly, as the computation is performed block by block instead of pixel by pixel.

The block size of the BLCM algorithm is chosen as the minimum required size to be detected. For instance, according to the above-mentioned damage standard, the size of the block is 15 mm × 15 mm. The image is divided into a series of blocks:

$$\text{Block}(i,j), \quad i = 1,2,\ldots,VN;\ \ j = 1,2,\ldots,HN \tag{5}$$

where VN and HN are the number of vertical and horizontal blocks, respectively.

For each block in the image, we define $\text{MeanB}(i,j)$ as the gray average of all pixels in the block:

$$\text{MeanB}(i,j) = \frac{1}{N^2}\sum_{x=x_a}^{x_a+N-1}\sum_{y=y_a}^{y_a+N-1} I(x,y) \tag{6}$$

where (x_a,y_a) is the coordinate of the top left corner point in this block, and I is the gray value of the image. We define $\text{MaxB}(i,j)$ as the maximum of the gray value in the block:

$$\text{MaxB}(i,j) = \max(I(pix)),\ \ pix \in \text{Block}(i,j) \tag{7}$$

For each $\text{Block}(i,j)$, there are eight neighboring blocks. We define m_1–m_8 as the gray average of each of these eight blocks, and the BLCM value of this block is

$$\text{BLCM}(i,j) = \min_k \frac{\text{MaxB}(i,j)\text{MeanB}(i,j)}{m_k}(k = 1,2,\ldots,8) \tag{8}$$

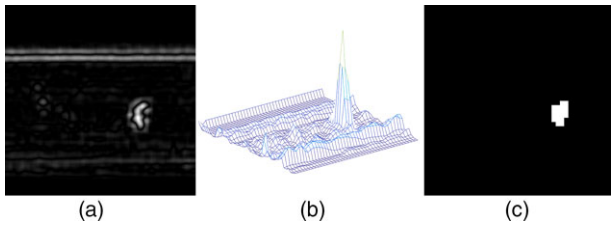

Fig. 2. Procedure of spalling detection: (a) image processed by 2D DoG filter, (b) the saliency map, and (c) the result of spalling detection

If this block and its surroundings are background areas, the difference between MeanBs of each block is small. Therefore we have $\max(m_k) > \mathrm{MaxB}(i,j)$, that is, $\mathrm{BLCM}(i,j) < \mathrm{MeanB}(i,j)$, and the background is suppressed.

If this block is the spalling area, the difference of MeanB between it and its neighbors is large. Then we get $\mathrm{BLCM}(i,j) > \mathrm{MeanB}(i,j)$. Thus the target is enhanced.

After processing by the BLCM algorithm, the target is enhanced and the background is suppressed, which conforms to the contrast mechanism in the visual saliency system. Thus the generated saliency map can be used to locate the spalling area. In case of mismatches when the spalling areas are just at the boundary of a block, the moving step of the block center is set to half of its side length.

2.2.3. Threshold discrimination In the saliency map *SaliM*, there is distinct difference between normal and spalling area. The last step is to distinguish them by setting a threshold:

$$Th = \frac{k\max(SaliM) + 2\min(SaliM)}{k+1} \tag{9}$$

where k is a parameter whose value depends on the quality of the surface image. Then blocks larger than Th will be considered as the spalling areas.

The procedure of spalling detection of a typical image is shown in Fig. 2.

As can be seen from the saliency map in Fig. 2(b), the spalling area reflects a high degree of saliency, while the high brightness contrast area on the top and the dotted stains on the left only reflect a very low degree of saliency. This reveals the two advantages of the BLCM algorithm: (i) It is not easily affected by nonuniform illumination. Traditional methods are based on gray scale, edge extraction, or contrast, so they are sensitive to gray scale changes caused by nonuniform illumination. The BLCM value proposed in this paper reflects the center–surround difference of a certain block. For large area of gray scale changes caused by nonuniform illumination, the BLCM value is relatively low. (ii) It is also not sensitive to the grain noises or stains. The size of the BLCM blocks is set according to the detecting requirements of the spalling areas, and the BLCM value calculation uses both the median and maximum gray values in the blocks, so it is not sensitive to the grain noises. The BLCM value is high only when the area is a spalling area with a certain size and unique image characteristics.

3. Experiment Results and Analysis

3.1. Threshold value analysis In this paper, the parameter k in Eq. (9) is empirically chosen for threshold value analysis experiments. To perform the threshold value analysis, we chose 100 images from the rail surface spalling detection dataset. The dataset used in this paper contains 200 images captured by four different line scan camera detection systems. The installation method of the line scan cameras and the angle of the auxiliary light sources affect the brightness distribution of the rail surface images. Light leakage from the side also has a great impact on the images especially when the rail surface is as smooth as mirror. In the dataset, the spalling areas longer than 15 mm are manually marked in advance for reference. The areas of the algorithm detected region (ADRA), the manually marked region (MMRA), and their overlap region (ORA) are calculated after detection. If ORA is less than 60% of ADRA, then it is regarded as false positive. If ORA is less than 60% of MMRA, then it is regarded as omission. Only images with neither false positive nor omission are regarded as correctly detected images.

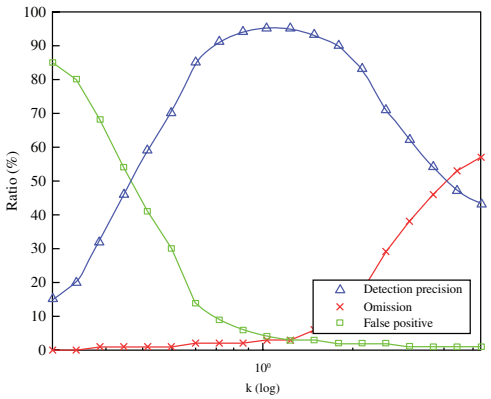

Fig. 3. Relationship between detection precision and k

In the experiment, the test value of k is increased by 20% each time from 0.2 to 5.32. The relationship between k and detection accuracy is shown in Fig. 3.

The threshold value analysis result shows that the detection acquires the best precision when k is equal to 1.1. Since the precision is higher than 90% when k is between 0.69 and 1.78, the model is not highly dependent on the value of k.

3.2. Algorithm robustness test In this section, the performance and robustness of the proposed algorithms are tested with three sets of experiments. The images used in the test are chosen from the rail surface spalling detection dataset, which are captured under different illumination and surface smoothness conditions.

Three algorithms are tested under the same condition for comparison. The DTA algorithm [18] uses dynamic threshold and the mean filter to locate possible spalling areas. Morphology operations are used to eliminate noise. The rail surface edges are determined by the longest two areas in the binary image, and the spalling areas are eventually recognized by their positions and sizes. As the edge positioning accuracy of the DTA algorithm is poor under complex illumination, we introduce another comparing algorithm, called MDTA, which applies DTA spalling detection after the rail surface positioning step of our algorithm. We also introduce a state-of-the-art saliency-based algorithm [22], called GBA. Since the GBA algorithm does not have the rail surface positioning step, we use our rail surface positioning result instead.

The detection results of all the four algorithms are compared with the manually marked results. The experimental results are shown in Figs 4–6. The correctly detected spalling areas, i.e. the overlap of ADRA and MMRA, are in white; the false positive regions are colored in cyan; and the omitted regions are colored in red.

In the result shown in Fig. 4, the rail surface positioning result of DTA is affected by the nonuniformity of illumination, and there are four correct detections: one false positive and one omission. MDTA locates all the five correct targets but has one false positive. GBA locates three correct targets but has one false positive and two omissions. In Fig. 5, DTA does not recognize the target on the

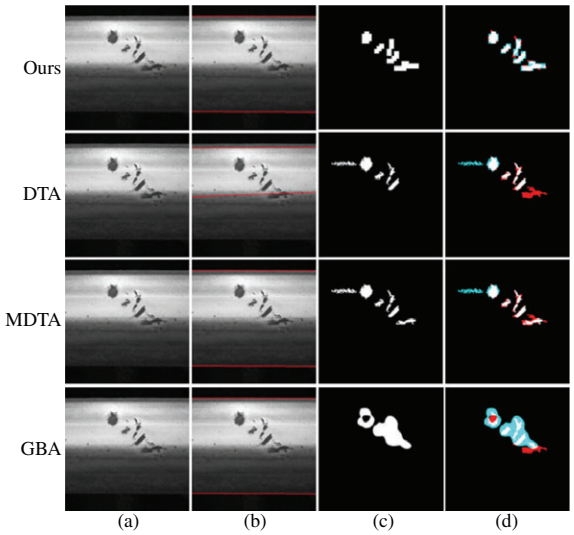

Fig. 4. First set of robustness test contrast experiment: (a) original image, (b) the result of rail surface positioning, (c) the result of spalling detection, and (d) the comparison of detection result and manually marked results

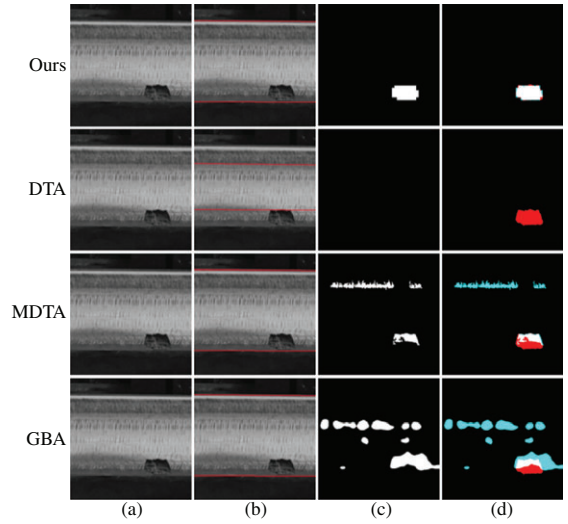

Fig. 5. Second set of robustness test contrast experiment: (a) original image, (b) the result of rail surface positioning, (c) the result of spalling detection, and (d) the comparison of detection result and manually marked results

edge, MDTA recognizes part of the target but has two more false positives, while GBA recognizes part of the target but has several false positives. In Fig. 6, the light-reflecting area is mistakenly considered as rail surface area by DTA, and hence it does not recognize the correct target. MDTA locates the correct target but has two false positives. GBA recognizes part of the target. In all the three experiments, our algorithm succeeds in locating the rail surface and detecting the targets accurately.

3.3. Spalling detection accuracy The evaluation of different algorithms requires a fair approach. The traditional rail surface spalling performance evaluation is done manually. The detection results of the equipment are rechecked by the railway maintenance workers in the field according to the railway maintenance principle of each country. The traditional manual evaluation method is susceptible to human factors, which is not fair for different algorithms. So we present an automatic modification of the traditional method to avoid the interference of human factors

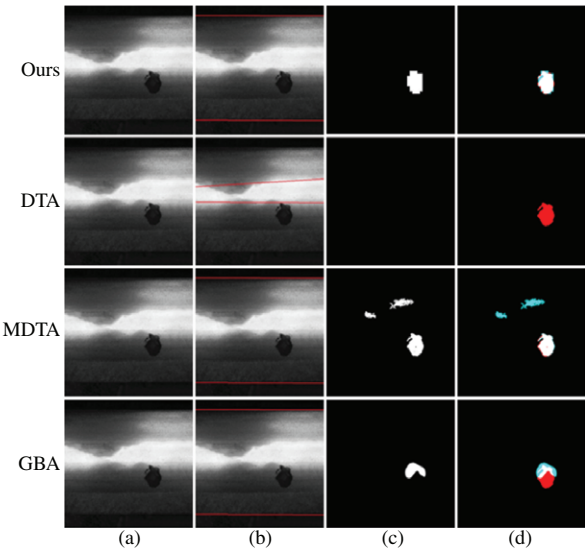

Fig. 6. Third set of robustness test contrast experiment: (a) original image, (b) the result of rail surface positioning, (c) the result of spalling detection, and (d) the comparison of detection result and manually marked results

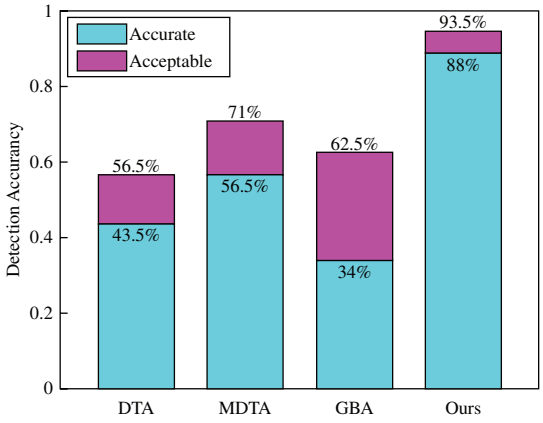

Fig. 7. Spalling detection accuracy

as far as possible. All the 200 images in the dataset are checked according to the railway maintenance principle, and the spalling areas longer than 15 mm is marked in advance. Whether the test results are accurate or not is determined by the overlapping ratio of the algorithm results and traditional reference results. The areas of ADRA, MMRA, and their ORA are calculated after detection. If ORA is more than 80% of both ADRA and MMRA, then the result is defined as accurate. If ORA is more than 60% of both ADRA and MMRA, and less than 80% of either ADRA or MMRA, then the result is defined as acceptable [24].

We also tested the accuracy of DTA, MDTA, and GBA algorithms. The test result is shown in Fig. 7.

The result demonstrates that our algorithm is much more accurate in spalling detection than the other three methods under test.

4. Conclusion

We proposed an optical rail surface spalling detection algorithm based on visual saliency. First, the rail surface area was located by Canny operator and Hough transformation to exclude the interference of the surrounding area. Then 2D DoG filter was used to reduce the noise. The filtered images were processed by means of a BLCM estimator, which could enhance the contrast of spalling

and normal area, to get the saliency map. Finally, a threshold was applied to locate the spalling area. Experimental results showed that, compared to three current methods, the proposed algorithm has good robustness and accuracy under different degrees of uniformity of illumination and various rail surface smoothness conditions. The detection accuracy of the proposed algorithm is about 22.5% higher than those of traditional methods under complex conditions.

Acknowledgments

This work was supported by the National Natural Science Foundation of China under Grant 61503288.

References

(1) Wang W, Guo H, Du X, Guo J, Liu Q, Zhu M. Investigation on the damage mechanism and prevention of heavy-haul railway rail. *Engineering Failure Analysis* 2013; **35**:206–218.
(2) Coccia S, Bartoli I, Marzani A, Lanza di Scalea F, Salamone S, Fateh M. Numerical and experimental study of guided waves for detection of defects in the rail head. *NDT & E International* 2011; **44**(1):93–100.
(3) Molyneux-Berry P, Davis C, Bevan A. The influence of wheel/rail contact conditions on the microstructure and hardness of railway wheels. *The Scientific World Journal* 2014; **2014**:209752.
(4) Clark R. Rail flaw detection: Overview and needs for future developments. *NDT & E International* 2004; **37**(2): 111–118.
(5) Lanza di Scalea F, Rizzo P, Coccia S, Bartoli I, Fateh M, Viola E, Pascale G. Non-contact ultrasonic inspection of rails and signal processing for automatic defect detection and classification. *Insight-Non-Destructive Testing and Condition Monitoring* 2005; **47**(6):346–353.
(6) Rizzo P, Cammarata M, Bartoli I, Scalea FLD, Salamone S, Coccia S, Phillips R. Ultrasonic guided waves-based monitoring of rail head: Laboratory and field tests. *Advances in Civil Engineering* 2010; **2010**:291293.
(7) Chillara VK, Lissenden CJ. Review of nonlinear ultrasonic guided wave nondestructive evaluation: Theory, numerics, and experiments. *Optical Engineering* 2016; **55**(1):011002.
(8) Bentoumi M, Aknin P, Bloch G. On-line rail defect diagnosis with differential eddy current probes and specific detection processing. *The European Physical Journal Applied Physics* 2003; **23**(03):227–233.
(9) Papaelias M, Ph CR, Davis CL. A review on non-destructive evaluation of rails: State-of-the-art and future development. *Proceedings of the Institution of Mechanical Engineers, Part F: Journal of Rail and Rapid Transit* 2008; **222**(4):367–384.
(10) Guoteng Z, Wang T, Ye J. Surface shape recognition method for crack detection. *Journal of Electronic Imaging* 2014; **23**(3):033013.
(11) Ma J, Zhao J, Tian J, Yuille AL, Tu Z. Robust point matching via vector field consensus. *IEEE Transactions on Image Processing* 2014; **23**(4):1706–1721.
(12) Loce RP, Bernal EA, Wu W, Bala R. Computer vision in roadway transportation systems: A survey. *Journal of Electronic Imaging* 2013; **22**(4):041121.
(13) Ma J, Chen C, Li C, Huang J. Infrared and visible image fusion via gradient transfer and total variation minimization. *Information Fusion* 2016; **31**:100–109.
(14) Mandriota C, Nitti M, Ancona N, Stella E, Distante A. Filter-based feature selection for rail defect detection. *Machine Vision and Applications* 2004; **15**(4):179–185.
(15) Lin J, Luo S, Li Q, Zhang H. Real-time rail head surface defect detection: A geometrical approach. *Industrial Electronics, 2009, ISIE 2009, IEEE International Symposium on*, IEEE, Seoul, 2009; 769–774.
(16) Nacereddine N, Hamami L, Oucief N. Non-parametric histogram-based thresholding methods for weld defect detection in radiography. *World Academy of Science, Engineering and Technology* 2005; **1**(9):213–217.
(17) Yuan X, Wu L, Chen H. Improved image preprocessing algorithm for rail surface defects detection. *Journal of Computer Aided Design & Computer Graphics* 2014; **26**(5):800–805.
(18) Liu Z, Wang W, Zhang X, Jia W. Inspection of rail surface defects based on image processing, *Informatics in Control, Automation and Robotics (CAR), 2010 2nd International Asia Conference on*, Wuhan, IEEE, 2010; Vol. 1, pp. 472–475.
(19) Laurent I, Koch C, Niebur E. A model of saliency-based visual attention for rapid scene analysis. *IEEE Transactions on Pattern Analysis & Machine Intelligence* 1998; **11**:1254–1259.
(20) Ma J, Zhao J, Tian J, Bai X, Tu Z. Regularized vector field learning with sparse approximation for mismatch removal. *Pattern Recognition* 2013; **46**(12):3519–3532.
(21) Chen CLP, Li H, Wei Y, Xia T, Tang YY. A local contrast method for small infrared target detection. *Geoscience and Remote Sensing, IEEE Transactions on* 2014; **52**(1):574–581.
(22) Sharma P. Modeling bottom-up visual attention using dihedral group D_4. *Symmetry* 2016; **8**(8):79.
(23) Nilufar S, Ray N, Zhang H. Object detection with DoG scale-space: A multiple kernel learning approach. *Image Processing, IEEE Transactions on* 2012; **21**(8):3744–3756.
(24) Ma J, Jiang J, Liu C, Li Y. Feature Guided Gaussian Mixture Model with Semi-Supervised EM and Local Geometric Constraint for Retinal Image Registration. *Information Sciences* 2017; **417**:128–142.

Zhixin Hu (Non-member) is currently a Lecturer with the School of Mechanical and Vehicular Engineering, Nanchang Institute of Science and Technology, China. He is also pursuing the Ph.D. degree at the School of Mechanical and Electrical Engineering, Nanchang University. His research interests include measurement and control technology of optical mechatronics.

Hongtao Zhu (Non-member) is now a Professor with the School of Mechanical and Electrical Engineering, Nanchang University. His research interests include measurement and control technology of optical mechatronics.

Ming Hu (Non-member) received the M.Sc. degree from South-Center University for Nationalities, China. She is now Dean of the College of Electrical and Information Engineering, Nanchang Institute of Science and Technology, China. Her research interests include electrical and information engineering.

Yong Ma (Non-member) graduated from the Department of Automatic Control, Beijing Institute of Technology, Beijing, China, in 1997, and received the Ph.D. degree from Huazhong University of Science and Technology (HUST), Wuhan, China, in 2003. Between 2004 and 2006, he was a Lecturer at the University of the West of England, Bristol, UK. Between 2006 and 2014, he was with the Wuhan National Laboratory for Optoelectronics, HUST, Wuhan, where he was a Professor of electronics. He is now a Professor with the Electronic Information School, Wuhan University. His general field of research is signals and systems. His current research interests include remote sensing using Lidar and infrared, as well as infrared image processing, pattern recognition, and interface circuits to sensors and actuators.